



Measuring CMB Spectral Distortions from Antarctica with COSMO: Blackbody Calibrator Design and Performance Forecast

L. Mele^{1,2} · E. S. Battistelli^{1,2} · P. de Bernardis^{1,2} · M. Bersanelli^{3,4} · F. Columbro^{1,2} · G. Coppi⁵ · A. Coppolecchia^{1,2} · G. D'Alessandro^{1,2} · M. De Petris^{1,2} · C. Franceschet^{3,4} · M. Gervasi^{5,6} · L. Lamagna^{1,2} · A. Limonta^{5,6} · E. Manzan³ · E. Marchitelli¹ · S. Masi^{1,2} · A. Mennella^{3,4} · F. Nati⁵ · A. Paiella^{1,2} · G. Pettinari⁷ · F. Piacentini^{1,2} · L. Piccirillo⁸ · G. Pisano¹ · S. Realini^{3,4} · C. Tucker⁹ · M. Zannoni^{5,6}

Received: 30 October 2021 / Accepted: 5 September 2022 / Published online: 26 September 2022
© The Author(s) 2022

Abstract

COSMO is a ground-based instrument to measure the spectral distortions (SD) of the Cosmic Microwave Background (CMB). In this paper, we present preliminary results of electromagnetic simulations of its reference blackbody calibrator. *HFSS* simulations provide a calibrator reflection coefficient of $R \sim 10^{-6}$, corresponding to an emissivity $\epsilon = 1 - R = 0.999999$. We also provide a forecast for the instrument performance by using an ILC-based simulation. We show that COSMO can extract the isotropic Comptonization parameter (modeled as $|y| = 1.77 \cdot 10^{-6}$) as $|y| = (1.79 \pm 0.19) \cdot 10^{-6}$, in the presence of the main Galactic foreground (thermal dust) and of CMB anisotropies, and assuming perfect atmospheric emission removal.

Keywords Cosmology · Spectral distortions · Blackbody

✉ L. Mele
lorenzo.mele@roma1.infn.it

¹ Università degli Studi di Roma “La Sapienza”, 00185 Roma, Italy

² INFN sezione di Roma, 00185 Roma, Italy

³ Università degli Studi di Milano, 20133 Milano, Italy

⁴ INFN sezione di Milano, 20133 Milano, Italy

⁵ Università di Milano - Bicocca, 20126 Milano, Italy

⁶ INFN sezione di Milano - Bicocca, 20126 Milano, Italy

⁷ INFN-CNR, 00156 Roma, Italy

⁸ Jodrell Bank Centre for Astrophysics, University of Manchester, Manchester M13 9PL, UK

⁹ School of Physics and Astronomy, Cardiff University, Queens Buildings, Cardiff CF243AA, UK

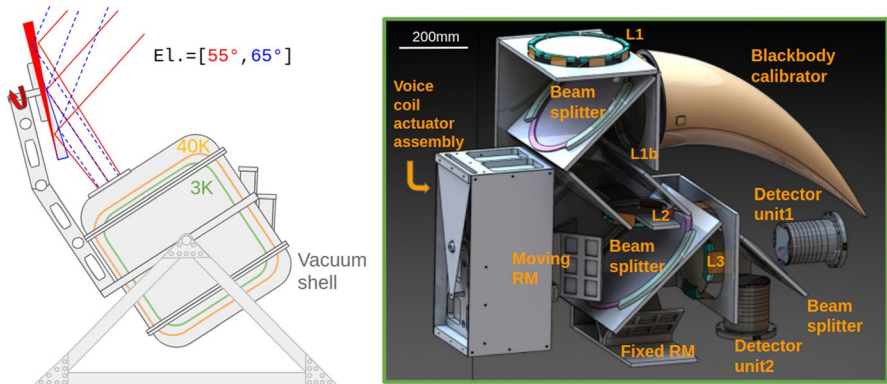


Fig. 1 Instrument schematic (left) and render of the cryogenic interferometer assembly within the 3K stage (right)

1 Introduction

COSMO (COSmic Monopole Observer) is a ground-based cryogenic differential Fourier transform spectrometer (DFTS) which aims at measuring the isotropic y -distortion of the Cosmic Microwave Background (CMB). Deviations from the almost-perfect blackbody spectrum are expected in the CMB and encode information on a wide variety of processes along the thermal history of the Universe, implying energy exchanges with CMB photons. These are both processes included in the standard Λ CDM model and ultra-high energy processes in the early Universe. Thus, the measurement of SDs represents a unique way of probing new physics [1]. To date, no isotropic SD have been detected at mm wavelengths and the upper limit for y is still $< 1.5 \cdot 10^{-5}$ [2, 3]. A cryogenic DFTS is ideally suited for CMB SD measurements, allowing for good control over systematic effects, and providing high common-mode rejection, $CMRR > 50$ dB [4]. COSMO will be operated at Dome-C, Antarctica, one of the best sites on Earth for CMB measurements due to the level of atmospheric stability [5].

2 Instrument

COSMO is a cryogenic DFTS. The cryostat consists in three main stages: the vacuum shell and the 40K and 3K stages, cooled down by two double-stage pulse tubes. The DFTS, reported in Fig. 1-right, is mounted on the 3K stage. One of the input ports of the DFTS faces the sky through a 220mm diameter Ultra-High Molecular Weight (UHMW) window [6] and a set of thermal filters limiting the thermal load. The other input port looks at a cryogenic blackbody calibrator. This is used as a reference and features low residual reflectance ($< 10^{-6}$), corresponding to an emissivity close to unity $\epsilon = 1 - 10^{-6} = 0.999999$. The DFTS is a traditional Martin–Puplett [7] completed by three lenses, L1 and L2 in Fig. 1 made of polyethylene, and L3 made of alumina. The two focal planes are equipped with

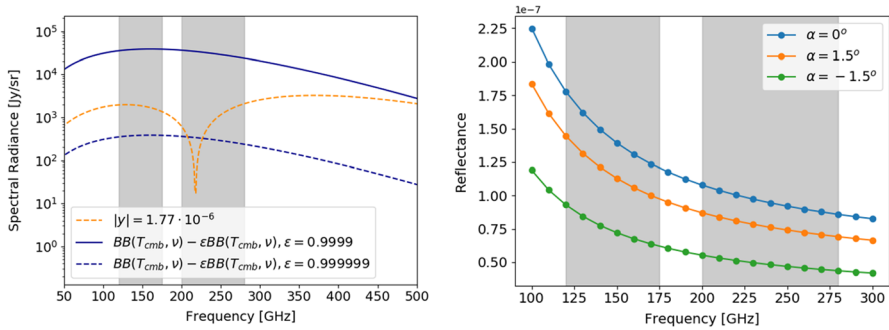


Fig. 2 Left panel: residual produced by a non-ideal blackbody cavity in a differential measurement of CMB isotropic γ distortion; the bias becomes subdominant as the emissivity approaches $\epsilon = 0.999999$. Right panel: residual cavity reflectance estimated for different incidence angles α at the cavity aperture, in the ray-tracing approximation, assuming a reflection coefficient of the cavity coating from [12]. The COSMO frequency bands are shaded in gray in the plot

multi-mode Kinetic Inductance Detectors (KIDs), 9 pixels for each array, sensitive in the 150 and 220GHz frequency bands, matching two high-transmission atmospheric windows. The focal planes are cooled down to 300mK via an ^3He evaporation cooler and the expected noise-equivalent-power (NEP) and time constant (τ) are $\text{NEP} \sim 3.8 \cdot 10^{-17} \text{W}/\sqrt{\text{Hz}}$ and $\tau \sim 60 \text{ms}$ [8, 9]. The interference is modulated by moving the DFTS roof-mirror via a voice coil actuator, which provides smooth and fast motion with almost no friction, minimizing the heat load on the 3K stage. The spectral resolution allowed by the cryogenic actuator ranges between 5 and 15GHz and the instrument *F.O.V.* is 1.5° . The atmospheric emission, with its fluctuations, is measured and removed by performing fast sky-dips using a spinning wedge mirror as the first optical train element. The 5° wedge mirror, 600mm in diameter, adds $\pm 5^\circ$ to the central elevation, rotating at maximum 2500rpm and collecting almost simultaneous data at different air masses within each 5s long interferogram. Proper data binning provides interferograms, and spectra, at different elevations. A schematic of the sky modulation is shown in Fig. 1-left, details on the instrument can be found in [10],

3 Blackbody Calibrator

A calibrator close to a perfect blackbody is needed for CMB SD measurements, to avoid spurious distortion signals. Assuming to perform a noise-free differential measurement of the CMB and the γ -distortion, comparing to a calibrator at the same temperature as the CMB and with an emissivity ϵ , a distortion signal arises as soon as the calibrator emissivity is $\epsilon < 1 - 10^{-6}$. In Fig. 2-left we report the distortion signal produced by a non-ideal blackbody calibrator: the spurious signal becomes subdominant for emissivity $\epsilon \geq 1 - 10^{-6}$.

The blackbody calibrator developed for COSMO is a single cone cavity deformed along a parabolic line, providing the absorption of input radiation through a large

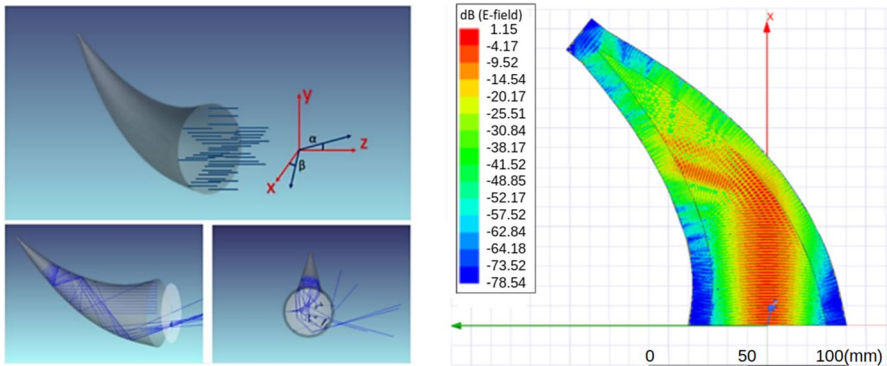


Fig. 3 Left panel: light rays trajectories within the parabolic blackbody cavity from *ZEMAX-Optic Studio*. Right panel: *HFSS* simulation of the electric field amplitude propagating within a few wavelengths thick slice of the cavity at 120GHz

number of interactions ($N > 6$) with the internal absorbing coating, and also limiting the diffraction produced by the apex of the cavity, whose size in its final section becomes comparable to the wavelength of the incident radiation. The calibrator has a 220mm aperture diameter and is 680mm long. The external body will be made of copper and the absorbing coating will be a 10mm thick layer of Eccosorb CR-110 (Emerson & Cuming), whose thermal and electromagnetic properties are well studied [11]. The thermal performance is still under optimization, however this design guarantees low thermal gradients given the material selected for the external body and thanks to several links which will thermally connect the cavity to the reference thermostat.

The *Optics-Studio ZEMAX*¹ software provides the performance in the geometrical optics approximation by counting the number of reflections of the input light against the cavity walls, assuming the reflectance properties of the CR110 coating as in [12], $r(\bar{\nu}) = 0.08 + \frac{0.06[\text{cm}^{-1}]}{\bar{\nu}}$, where $\bar{\nu}$ is the wave number. Input light rays undergo $N > 6$ reflections with the coating, corresponding to a residual reflectance $R < 10^{-6}$ over the band 100-300GHz. The estimated reflectance of the cavity is reported at different incidence angles α in Fig. 2-right, within the DFTS *F.O.V.*, and provides an emissivity $\epsilon > 0.999999$. The rays trajectories are reported in Fig. 3-left. The cavity performance has been also assessed via *Ansys HFSS*² electromagnetic simulations. Given the size of the calibrator and the frequencies to be explored, only a few wavelengths thick slice of the calibrator, scaled by a factor of 3, has been included in the simulation. As a result, the simulation is representative in terms of the absorbing properties of the cavity, but is not representative of the direction of the damped outgoing radiation. The simulations have been run only for the lower frequency of the 150GHz band. The dielectric properties of the coating at 120GHz are relative

¹ Optics-Studio ZEMAX <https://www.zemax.com/pages/opticstudio>.

² Ansys HFSS <https://www.ansys.com/it-it/products/electronics/ansys-hfss>.

permittivity $\epsilon_r = 3.67$ and dielectric loss tangent $\tan\delta = 0.03$ [13]. The input radiation is set as an incident Gaussian beam, determined by the lens L1b coupled with the calibrator. The electric field amplitude within the cavity is reported in Fig. 3-right. The reflectance, computed as the ratio of the Poynting vector fluxes of the scattered and incident radiation, is $R(120GHz) = 3.2 \cdot 10^{-6}$.

The discrepancy in the determination of R is mainly dictated by diffractive effects, which are neglected in the geometric approximation, and by the corresponding reflection coefficient used to derive the reflectance in the ray-tracing approach, which was measured at normal incidence in [12]. No bias from the blackbody calibrator is included in the forecast simulation, as for $R = 3.2 \cdot 10^{-6}$ the bias is still subdominant in the two frequency bands.

4 Performance Forecast

The performance of the instrument is assessed via ILC (Internal Linear Combination)-based simulations. ILC methods exploit multi-frequency input maps to separate the map of the signal of interest from other components emitting in a sky region, exploiting the knowledge of their spectral shape. A constrained-ILC (c-ILC) [14] is applied to simulated sky maps, given by the superposition of the PySM [15] realizations of CMB anisotropies and thermal dust emission, as the main galactic foreground. The distortion map is added as an isotropic Compton- y map with $y = 1.77 \cdot 10^{-6}$, converted in brightness units Jy/sr. The input multi-frequency maps, with a spectral resolution $\Delta\nu = 10GHz$, are absolutely calibrated maps, with a map resolution parameter $N_{side} = 64$. Noise realizations are added as Gaussian noise, dominated by the photon noise from the cryostat window emission, taken as a gray-body with 1% emissivity and at 220K, and by the atmospheric emission, based on the *a.m.* software [16] with precipitable-water-vapor PWV=0.15mm. The measurements will be taken at fixed elevation $el. = 60^\circ$ of the cryostat axis. This, combined with the sky modulation from the spinning wedge mirror, results in the observation of a fraction of the sky where 11 independent sky patches 15° in diameter are selected, as shown in Fig. 4-left. For illustrative purposes we show in the red box in the figure the coverage map produced by a slowed 0.0010Hz wedge mirror modulation in 2h.

Assuming 1year of observations with $\eta = 30\%$ time-efficiency, the corresponding error per $1deg^2$ pixel and per spectral bin is evaluated from [17] as 110Jy/sr and 323Jy/sr, for the 150 and 220GHz bands, respectively. We assume a perfect atmospheric emission removal by the fast sky-dips procedure.

In the c-ILC machinery different orders of the thermal dust emission moment expansion are subtracted from the solution as in [18], to limit biases produced by the superposition of multiple dust populations and effects of averaging within the instrumental beam, which would produce unwanted distortion signals. The c-ILC y solution maps of the first patch are reported in Fig. 4-middle, where the 0^{th} order of the thermal dust emission and of CMB anisotropies are subtracted in the middle-top map, while up to the first derivative of the thermal dust emission is subtracted in the middle-bottom map. The second solution shows a variance

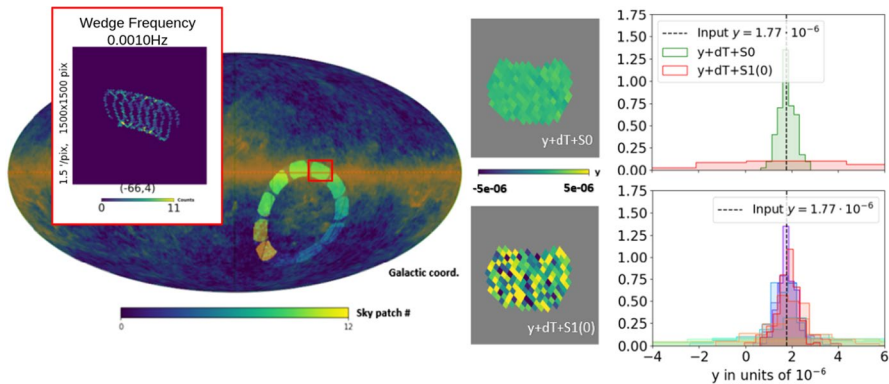


Fig. 4 Left: COSMO coverage map superimposed over the 270GHz thermal dust PySM map. Middle: output y maps of the sky patch # 1 from the c-ILC solution where the 0^{th} order of the thermal dust emission and the CMB anisotropies are removed from the solution (top) and where up to the first-order moment of the thermal dust emission (bottom) is removed. Right: Histograms of the y maps from different c-ILC solutions for the sky patch # 1 (top) and from the best c-ILC solutions over the 11 sky patches

degradation of the map as the higher orders of dust emission are subtracted. Histograms of the output Compton- y maps, reported in Fig. 4 top-right for the sky patch # 1, also show that the best c-ILC solution is provided by the first solution. A weighted average of the independent y distortion estimates over the 11 sky patches, evaluated from the histograms in Fig. 4 bottom-right from the best c-ILC solutions, shows that COSMO can extract the isotropic comptonization parameter as $|y| = (1.79 \pm 0.19) \cdot 10^{-6}$.

The efficiency of the method is related to the noise level and the available frequency coverage, which are both limited and prevent the efficient removal of higher orders of the thermal dust emission for a ground-based implementation.

5 Conclusions

We presented preliminary simulations of the blackbody reference signal for CMB y -distortion measurements. We developed a blackbody cavity whose geometry maximizes the absorption of input radiation and limits the effect of diffraction. *HFSS* simulations forecast a residual reflectance $R = 3.2 \cdot 10^{-6}$ at 120GHz, corresponding to an emissivity $\epsilon \simeq 0.999999$, limiting the spurious distortion signal. We assessed the performance of COSMO via ILC-based simulations, showing that the isotropic comptonization parameter is extracted as $|y| = (1.79 \pm 0.19) \cdot 10^{-6}$ in the presence of foreground thermal dust emission and CMB anisotropies, assuming a perfect atmospheric emission removal and a noise realization dominated by the photon noise from the atmosphere and the cryostat window.

Funding Open access funding provided by Università degli Studi di Roma La Sapienza within the CRUI-CARE Agreement.

Declarations

Conflicts of interest This research received PNRA and PRIN grants. The Authors declare that there are no conflicts of interest.

Open Access This article is licensed under a Creative Commons Attribution 4.0 International License, which permits use, sharing, adaptation, distribution and reproduction in any medium or format, as long as you give appropriate credit to the original author(s) and the source, provide a link to the Creative Commons licence, and indicate if changes were made. The images or other third party material in this article are included in the article's Creative Commons licence, unless indicated otherwise in a credit line to the material. If material is not included in the article's Creative Commons licence and your intended use is not permitted by statutory regulation or exceeds the permitted use, you will need to obtain permission directly from the copyright holder. To view a copy of this licence, visit <http://creativecommons.org/licenses/by/4.0/>.

References

1. J. Chluba et al., Astro2020 Science White Paper (2019). [arXiv:1903.04218](https://arxiv.org/abs/1903.04218)
2. D.J. Fixsen et al., *ApJ* **581**, 817 (2002). <https://doi.org/10.1086/344402>
3. M. Gervasi et al., *ApJ* **688**, 24 (2008). <https://doi.org/10.1086/592134>
4. G. D'Alessandro et al., *Appl. Opt.* **54**, 9269–9276 (2015). <https://doi.org/10.1364/AO.54.009269>
5. P. Tremblin et al., *A & A* **535**, A112 (2011). <https://doi.org/10.1051/0004-6361/201117345>
6. G. D'Alessandro et al., *Infra. Phys. & Tech.* **90**, 59–65 (2018). <https://doi.org/10.1016/j.infrared.2018.02.008>
7. D.K. Lambert et al., *Appl. Opt.* **17**, 1595–1602 (1978). <https://doi.org/10.1364/AO.17.001595>
8. A. Paiella et al., *J. Phys.: Conf. Ser.* **1182**, 012005 (2019). <https://doi.org/10.1088/1475-7516/2019/01/039>
9. A. Paiella et al., *J. Low Temp. Phys.* **199**, 491–501 (2020). <https://doi.org/10.1007/s10909-020-02372-y>
10. S. Masi et al., (2021). Proceedings of the 16th Marcel Grossmann Meeting <https://doi.org/10.48550/arXiv.2110.12254>
11. H. Hemmati et al., *Appl. Opt.* **24**, 4489–4492 (1985). <https://doi.org/10.1364/AO.24.004489>
12. J.C. Mather et al., *ApJ* **512**, 511–520 (1999). <https://doi.org/10.1086/306805>
13. J.W. Lamb, *Int. J. Infrared Milli. Waves* **17**, 1997–2034 (1996). <https://doi.org/10.1007/BF02069487>
14. M. Remazeilles et al., *Mon. Notices Royal Astron. Soc.* **410**, 4 (2011). <https://doi.org/10.1111/j.1365-2966.2010.17624.x>
15. B. Thorne et al., *Mon. Notices Royal Astron. Soc.* **469**, 2821–2833 (2017). <https://doi.org/10.1093/mnras/stx949>
16. S. Paine, *Am. Atmos. Model.* (2019). <https://doi.org/10.5281/zenodo.640645>
17. P. de Bernardis et al., *A & A* **538**, A86 (2012). <https://doi.org/10.1051/0004-6361/201118062>
18. A. Rotti et al., *Mon. Notices Royal Astron. Soc.* **500**, 1 (2021). <https://doi.org/10.1093/mnras/staa3292>

Publisher's Note Springer Nature remains neutral with regard to jurisdictional claims in published maps and institutional affiliations.